⌘ *Author's Choice*

iTRAQ-based Proteomics Profiling Reveals Increased Metabolic Activity and Cellular Cross-talk in Angiogenic Compared with Invasive Glioblastoma Phenotype*[S]

Uros Rajcevic‡, Kjell Petersen§, Jaco C. Knol¶, Maarten Loos‖, Sébastien Bougnaud‡, Oleg Klychnikov‖, Ka Wan Li‖, Thang V. Pham¶, Jian Wang, Hrvoje Miletic**, Zhao Peng**, Rolf Bjerkvig‡**, Connie R. Jimenez¶, and Simone P. Niclou‡ ‡‡**

Malignant gliomas (glioblastoma multiforme) have a poor prognosis with an average patient survival under current treatment regimens ranging between 12 and 14 months. The tumors are characterized by rapid cell growth, extensive neovascularization, and diffuse cellular infiltration of normal brain structures. We have developed a human glioblastoma xenograft model in nude rats that is characterized by a highly infiltrative non-angiogenic phenotype. Upon serial transplantation this phenotype will develop into a highly angiogenic tumor. Thus, we have developed an animal model where we are able to establish two characteristic tumor phenotypes that define human glioblastoma (*i.e.* diffuse infiltration and high neovascularization). Here we aimed at identifying potential biomarkers expressed by the non-angiogenic and the angiogenic phenotypes and elucidating the molecular pathways involved in the switch from invasive to angiogenic growth. Focusing on membrane-associated proteins, we profiled protein expression during the progression from an invasive to an angiogenic phenotype by analyzing serially transplanted glioma xenografts in rats. Applying isobaric peptide tagging chemistry (iTRAQ) combined with two-dimensional LC and MALDI-TOF/TOF mass spectrometry, we were able to identify several thousand proteins in membrane-enriched fractions of which 1460 were extracted as quantifiable proteins (isoform- and species-specific and present in more than one sample). Known and novel candidate proteins were identified that characterize the switch from a non-angiogenic to a highly angiogenic phenotype. The robustness of the data was corroborated by extensive bioinformatics analysis and by validation of selected proteins on tissue microarrays from xenograft and clinical gliomas. The data point to enhanced intercellular cross-talk and metabolic activity adopted by tumor cells in the angiogenic compared with the non-angiogenic phenotype. In conclusion, we describe molecular profiles that reflect the change from an invasive to an angiogenic brain tumor phenotype. The identified proteins could be further exploited as biomarkers or therapeutic targets for malignant gliomas.   *Molecular & Cellular Proteomics 8:2595–2612, 2009.*

Glioblastoma multiforme (GBM)[1] is the prevalent and most fatal brain tumor in adults with an average patient survival time between 12 and 14 months under current treatment regimens. Invasion and angiogenesis are two defining hallmarks of GBM that are largely responsible for the aggressive nature of the disease (1). Invasion is likely triggered by signals that prompt tumor cells to egress from the tumor mass, including those that are activated by an acidic and hypoxic environment (*e.g.* hypoxia-inducible factor) (2). These highly infiltrative glioma cells escape neurosurgical resection and are the seeds for tumor recurrence. Oxygen limitation in the tumor microenvironment is also responsible for the active recruitment of new blood vessels from preexisting vessels, a process termed angiogenesis. Absence of angiogenesis is considered a rate-limiting factor in solid tumors. Although high grade gliomas show extensive infiltration of the normal brain they are also among the neoplasms with the highest degree of

[1] The abbreviations used are: GBM, glioblastoma multiforme; iTRAQ, isobaric tags for relative and absolute quantitation; TMA, tissue microarray; EGFR, epidermal growth factor receptor; SCX, strong cation exchange; CI, confidence interval; NCBI, National Center for Biotechnology Information; CA, correspondence analysis; 2D, two-dimensional; FDR, false discovery rate; VEGF, vascular endothelial growth factor; S, supernatant; P, patient; ID, identification; Anx, Annexin; GO, gene ontology; MHC, major histocompatibility complex.

vascularization (3–5). Antiangiogenic treatment is considered a promising therapeutic strategy against malignant brain tumors and is currently being evaluated in clinical trials (6).

In solid tumors the angiogenic switch is thought to occur when the balance between proangiogenic and antiangiogenic molecules is shifted in favor of angiogenesis, permitting rapid tumor growth and subsequent development of invasive and metastatic properties (7). Thus, aggressive tumor growth depends on a successful adaptation of the tumor cells to the host microenvironment. In brain tumors no biomarkers are currently available that define different cell populations within human GBMs (for instance tumor cells that show infiltrative growth and those that trigger angiogenesis) or that predict the propensity of low grade (non-angiogenic) gliomas to develop into malignant angiogenic gliomas. We have recently generated a xenograft model for human GBM that displays a highly invasive phenotype and stem cell characteristics (8). By serial transplantation in nude rats new cell clones eventually develop that generate a more rapidly growing aggressive, angiogenesis-dependent phenotype. The transition to an angiogenic phenotype is accompanied by a reduced infiltrative growth (8). Thus, we are able to initiate two distinct phenotypes from human GBMs that classify their growth and progression. Our model is extremely useful for identifying mechanisms causing the switch from angiogenesis-independent to angiogenesis-dependent tumor growth.

This work was aimed at identifying cell membrane markers and molecular pathways that characterize the two phenotypes and may underlie the angiogenic switch. Such markers may represent potential therapeutic targets toward specific cellular subsets within GBMs. Here we applied iTRAQ peptide labeling on membrane-enriched tumor fractions followed by MALDI-TOF/TOF protein identification and bioinformatics analysis to quantify large scale species-specific protein expression over four consecutive generations of the glioma xenograft model.

In a search for disease biomarkers, there has been a rapid development of quantitative protein expression technologies including isobaric peptide tagging (iTRAQ) combined with multidimensional LC and MS/MS analysis (9). This approach allows for sample multiplexing (currently 4- or 8-plex at the time). iTRAQ is particularly powerful when applied on a subfraction of the proteome, thereby increasing the possibility of identifying less abundant proteins (10). Because more than a third of all known biomarkers as well as more than two-thirds of known and potential antitumor protein targets are membrane-related proteins (11–14), we focused on membrane-enriched fractions of the tumor xenografts. In four different iTRAQ experiments we were able to identify over 7000 (redundant) proteins of which 1460 proteins were extracted based on quantifiable and species-specific expression. Correspondence analysis and unsupervised cluster analysis confirmed consistent protein expression profiles in the different

xenograft phenotypes generated from different patient samples. The expression of a selection of identified candidates was confirmed by immunohistochemical methods on tissue microarrays (TMAs) from a large number of xenograft tumors and patient gliomas. The differentially expressed proteins identified in the two phenotypes represent unique candidate biomarkers that may represent novel therapeutic targets in GBMs. The information generated also provides novel insight into the molecular networks governing the infiltrative and the angiogenic tumor properties and reveals new mechanisms involved in the angiogenic switch in GBMs.

EXPERIMENTAL PROCEDURES
Animal Model

Human tumor spheroids derived from GBM biopsies were cultured for 10–14 days on agar-coated flasks in serum-containing medium and transplanted into the brain of nude rats as described previously (8, 15, 16). First generation rats developed highly invasive tumors that were lethal within 3–4 months. Tumor spheroids generated from the first generation xenografts were transplanted into subsequent generations of rats. After serial passaging in rats over 4–6 generations, the tumors gradually underwent an adaptation to the host characterized by a more aggressive angiogenic phenotype (see Fig. 1). Brain tumor xenografts thus generated over four generations of rats from two different patient GBMs (patients 6 and 17) were collected, flash frozen in liquid nitrogen, and stored at $-80\ ^\circ C$ until further processing. The handling of the animals and the surgical procedures were performed in accordance with the Norwegian Animal Act, and the local ethics committee approved the protocol. The biopsy material was obtained from the Department of Neurosurgery, Haukeland University Hospital, Bergen, Norway. All biopsies were primary GBMs (patient 6 (P6), 81-year-old female; P7, 64-year-old male) with epidermal growth factor receptor (EGFR) amplification. The collection of tumor tissue was approved by the regional ethics committee at Haukeland University Hospital, Bergen, Norway.

Tissue Processing and Fractionation

Membrane fractions were prepared as described previously (17). Briefly tissue samples were homogenized with a Polytron homogenizer (Kinematica, Lucerne, Switzerland) in 10 ml of 0.32 M sucrose, 5 mM HEPES, pH 7.4, protease inhibitor mixture (Amersham Biosciences)/g of tissue. The homogenate was centrifuged for 10 min at $1000 \times g$ at 4 °C to remove the cell debris. Supernatant 1 (S1) was collected and centrifuged for 30 min at 4 °C on a tabletop centrifuge at $16,000 \times g$. An aliquot of it was saved for quality control (see Fig. 2). The resulting pellet was homogenized in the same buffer (0.32 M sucrose, 5 mM HEPES, pH 7.4, protease inhibitor mixture (Amersham Biosciences)) and centrifuged for 30 min at 4 °C at $20,000 \times g$. The resulting pellet (the crude membrane fraction) was resuspended in a buffer containing 0.32 M sucrose, 5 mM NaH_2PO_4, pH 8.1, protease inhibitor mixture (Amersham Biosciences), and supernatant 2 (S2) was saved for quality control. A sucrose step gradient was formed in a 17-ml ultracentrifuge tube (Beckman Coulter, Fullerton, CA) with 1.4 M sucrose in water at the bottom followed by a layer of 1.1 M sucrose. The crude membrane fraction was applied at the top. The tubes were centrifuged at $85,000 \times g$ (Beckmann SW 40 rotor, Beckman Coulter) for 2 h at 4 °C. The two layers between 0.32 and 1.1 M sucrose (light membranes) and between 1.1 and 1.4 M sucrose (plasma membranes), respectively, were carefully collected and centrifuged at $86,000 \times g$ (SW31T1–1 rotor, Beckman Coulter) at 4 °C for 2 h. The two pelleted membrane fractions were resuspended in 5 mM HEPES,

pH 8.1. Protein concentration in the homogenate, S1, S2, and membrane suspensions was estimated using Bradford reagent (Bio-Rad) and absorbance measurement at 595 nm.

Western Blot Analysis

Proteins samples dissolved in SDS sample buffer were separated by SDS-PAGE and transferred to a PVDF membrane (Bio-Rad). EGFR (Chemicon, Temecula, CA) and actin antibody binding was revealed with the ECL Plus Western Blotting Detection system (Amersham Biosciences) according to the manufacturer's instructions.

Sample Labeling

Sample labeling with isobaric tagging reagents was carried out according to the manufacturer's instructions with modifications (iTRAQ® Reagents Multiplex kit; Applied Biosystems/MDS Sciex, Foster City, CA). Briefly 100 μg of membrane suspensions was vacuum-dried, resuspended in 25 μl of Rapigest detergent solution (Waters) dissolved in 125 μl of Dissolution buffer from the iTRAQ kit per vial of detergent, and vortexed. 2 μl of reducing agent (Applied Biosystems/MDS Sciex) was added followed by incubation with vortexing for 2 h at room temperature. After centrifugation, cysteine-blocking agent was added and incubated for 10 min at room temperature followed by addition of 2 μg of trypsin (modified sequencing grade; Promega, Madison, WI) and incubation for 12 h at 37 °C. Digested samples were labeled with four different iTRAQ reagents dissolved in 80 μl of ethanol and vortexed at room temperature for 4 h. After the labeling, the four samples were pooled, 400 μl of 1% (v/v) TFA was added to cleave the Rapigest detergent, and samples were vortexed for 1 h at room temperature and centrifuged. The supernatant was removed and vacuum-dried. Four separate quadruplex iTRAQ experiments were performed. 1) In iTRAQ1 light membranes from early and late generations of two different GBM patients (P6 and P17) were analyzed with P6 first and last labeled with iTRAQ 114 and 115, respectively, and P17 first and last labeled with iTRAQ 116 and 117, respectively. 2) In iTRAQ2 plasma membranes of the same samples were analyzed. 3) and 4) In iTRAQ3 and iTRAQ4 plasma membranes from four consecutive generations of xenografts originating from the two GBM patients (P6 and P17, respectively) were analyzed. Samples were labeled as follows: iTRAQ 114, first (early); iTRAQ 115, second; iTRAQ 116, third; and iTRAQ 117, fourth (late) generation. The experimental flowchart is summarized in Fig. 2.

Two-dimensional Liquid Chromatography

The iTRAQ labeled peptide pool was resuspended in 170 μl of buffer A (10 mM KH$_2$PO$_4$, 20% (v/v) acetonitrile, pH 2.9) and separated on a strong cation exchange (SCX) column (PolySULFOETHYL Aspartamide, 100 × 2.1 mm, 3 μm, 300 Å (Poly LC, Columbia, MD)) under the following conditions: flow, 200 μl, 20-min gradient, 0–60% B (A + 500 mmol KCl); 5 min, 60–100% B; 4 min, 100% B. Minute fractions were collected in a fraction collector and vacuum-dried. 20 peak SCX fractions were dissolved in 30–60 μl of 0.1% (v/v) TFA and further separated on a microcapillary reverse phase column (Repro-Sil-Pur C$_{18}$ Aqua 3-μm material, 100-μm-inner diameter, 15-cm column) under the following conditions: flow, 400 μl; buffer A, 5% (v/v) acetonitrile, 0.05% (v/v) TFA; buffer B, 80% (v/v) acetonitrile, 0.04% (v/v) TFA; 6 min, 5% B; 45 min, 5–45% B; 1 min, 45–90% B; 5 min, 90% B; 1 min, 90–5% B. The reverse phase fractions were premixed with the matrix (6 mg/ml α-cyanohydroxycinnaminic acid in 33.3% (v/v) acetonitrile, 1 mM ammonium citrate) and spotted on line onto a MALDI target plate using a Probot Microfraction Collector (Dionex, Sunnyvale, CA). 192 spots were spotted per fraction.

MALDI-TOF-TOF Mass Spectrometry

For all measurements, a 4800 MALDI-TOF/TOF Analyzer (Applied Biosystems/MDS Sciex) operated under 4000 Series Explorer v.3.5.1 software (Applied Biosystems/MDS Sciex) was used. The instrument was equipped with a 20-μJ neodymium-doped yttrium aluminium garnet (Nd-YAG) laser operating at 355 nm and 200 Hz and was used in reflector-positive ion mode. For calibration and tuning purposes, 4700 Cal Mix (Applied Biosystems/MDS Sciex) containing six calibrant peptides in the m/z range of 904–3658 were spotted on 13 dedicated calibration spot locations distributed over each MALDI target plate. Before each job run, the instrument was retuned (including deflector, mirror, time ion selector, and laser settings), and MS and MS/MS default calibration was updated. Automatic jobs were created for two 384-spot MALDI target plates at a time. In MS analyses, 1250 shots (25 subspectra at randomized locations over the whole spot, 50 shots/spectrum) were acquired and averaged over an m/z window of 800–4000. For each spot, up to 30 of the strongest precursor peaks with a minimal signal-to-noise ratio of 35 were automatically selected for MS/MS analysis using a job-wide interpretation method that excludes multiple analyses of the same precursor with a 200-ppm tolerance. In MS/MS analyses, acquisition was from the weakest to the strongest selected precursor for each spot. For each precursor, 2500 shots (50 subspectra at randomized locations over the whole spot, 50 shots/spectrum) were acquired and averaged. All MS/MS fragmentation (collision-induced dissociation) was performed with air at medium pressure ($\sim$1 × 10^{-6} torr) and using 2-keV collision energy.

Analysis of the Spectra and Extraction of Species-specific Proteins

MS/MS spectra were searched against databases with trypsin specificity, allowing one missed cleavage and fixed iTRAQ modifications at lysine residues and the N termini of the peptides, using GPS Explorer v.3.6. (Applied Biosystems/MDS Sciex), which incorporates the Mascot (v.2.1.) search algorithm (Matrix Science Inc., Boston, MA). Mass tolerance was set to 100 ppm for precursor ions and 0.5 Da for fragment ions. The Mascot confidence interval (CI) in percent was calculated by GPS Explorer (Applied Biosystems/MDS Sciex) based on the Mascot ion scores. Because peptides could have been derived from rat (host) or human (tumor) proteins, spectra were annotated twice using the peptides with the highest Mascot CI, once according to the rat Swiss-Prot database and once according to the human Swiss-Prot database (UniProtKB/Swiss-Prot Release 9.6 of February 6, 2007 (Swiss-Prot Release 51.6)). If a spectrum was not annotated using the well curated rat or human Swiss-Prot databases, Mascot searches were performed in the larger but more redundant NCBI rat and human databases (NCBInr release of March 29, 2005). Next the precursor protein sequences of all peptides were retrieved from the respective databases, and NCBI sequences that shared more than 90% similarity over 85% of the sequence length with a Swiss-Prot sequence were clustered together as a single protein cluster (blastclust). Clustering of Swiss-Prot sequences was not permitted, thereby preventing the clustering of human and rat sequences. Next the sequences of the peptides were compared with the sequence of the protein clusters. Peptides were automatically compared with a protein cluster using the VBA script in Excel. Using a text search, the peptide sequences were searched in the sequences of all proteins of a cluster. Peptides were only matched to a protein cluster if the protein sequence was preceded by an Arg or Lys (trypsin cleavage sites) or if the peptide sequence started with a Met and matched to the beginning of a protein sequence. Peptides that matched the sequence of more than one cluster were considered species- or isoform-nonspecific. These nonspecific peptides were not considered for protein identification and quantification. Peak areas for

each iTRAQ signature peak (*m/z* 114.1, 115.1, 116.1, and 117.1) were obtained directly from the Oracle database of the mass spectrometer, corrected according to the manufacturer's instructions to account for the differences in isotopic overlap, and $\log_2$-transformed. Possible systematic differences in the starting amounts or labeling efficiencies between samples were normalized by subtracting the mean peak area of a sample from each individual iTRAQ signature peak. Low signature peaks generally have larger variation, which may compromise the quantitative analysis of the proteins. Therefore, peptides with iTRAQ signature peaks less than 10.97 ($\log_2$) were not considered for quantification. To compare the abundance of peptides across multiple iTRAQ experiments, within each experiment peptide quantity values were standardized to scores around zero by subtracting the mean peak area of all four samples. These normalized and standardized peptide quantity values were used to calculate mean protein quantity values.

Data Analysis in J-Express

The mean protein quantity values were imported into J-Express v.2.8 (18, 19) for further analysis. Only proteins quantified by at least two peptides in all four iTRAQ signature peaks and having at least one peptide with better Mascot CI value of 95% were imported for quantitative analysis. Note that because data sets from four different iTRAQ experiments were combined, one particular protein can be present up to four times in the final (redundant) data set. Except to calculate mean -fold changes, the separate entry points for one protein were not combined to be able to attribute each data point to the corresponding iTRAQ experiment from which it was derived.

Difference in Protein Abundance Levels—A protein quantity value matrix was formed having four columns representing the following xenograft samples: 1) early generation P6, 2) late generation P6, 3) early generation P17, and 4) late generation P17. Quality filtered data from iTRAQ1 and iTRAQ2 fitted directly into this matrix with different proteins on separate rows. From iTRAQ3 and iTRAQ4 (P6 and P17, respectively) the standardized early and late generation xenograft samples (labels 113 and 117, respectively) protein quantity values were added as additional rows in the protein quantity matrix. To identify consistent differences in protein abundance levels in both P6 and P17 between the early and late generation, we applied the RankProduct method (20) implemented in J-Express. RankProduct is a robust approach designed for experiments with few replicates and provides false discovery rate-equivalent *q* values as confidence estimates to counter for the issues of multiple testing in high throughput experiments.

Correspondence Analysis (CA) Plots—To visualize a global view of how the samples and proteins relate to each other, the CA approach (21) calculates the principal components of both the sample co-variance matrix and the protein co-variance matrix in such a manner that the resulting most significant principal components can be used to plot both samples and proteins in the same biplot. The biplot thus provides a 2D estimated global view of sample-sample, sample-protein, and protein-protein relationships found in the original higher order dimension data set.

Trend Analysis over Four Generations—The quality filtered data of iTRAQ3 and iTRAQ4, representing the four xenograft generations of P6 and P17, respectively, were imported as two separate data sets in J-Express. Unsupervised analysis approaches like self-organizing map clustering (22) and Profile similarity search were utilized to identify candidate trend profiles over the four generations in each of the two experiments. For biological interpretation of proteins sharing a trend profile, overlap sets were calculated, and annotations were manually inspected.

Immunohistochemistry

Immunostaining on Formalin-fixed Paraffin-embedded Tissue Sections—Immunohistochemical stainings were revealed with the Dako
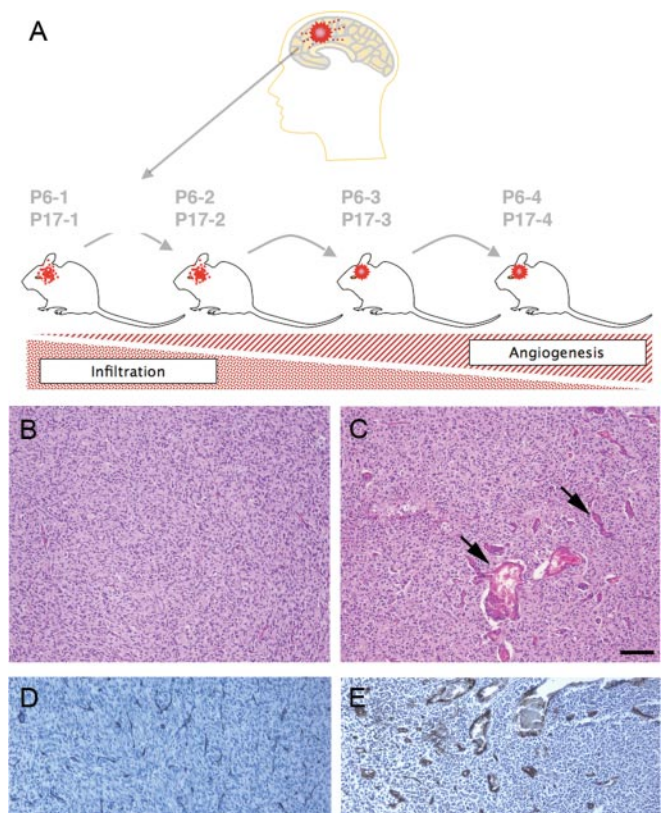

FIG. 1. **Orthotopic xenograft brain tumor model.** *A*, schematic presentation of transplantation experiments and the phenotypes that developed. *B*, histological section of the invasive early generation phenotype growing in the nude rat brain. *C*, by serial passage in several generations of rats, the tumor develops into a highly angiogenic phenotype. *Arrows* point to large pathological vessels abundant in the late generation tumors (hematoxylin and eosin staining; *bar*, 500 μm). Immunostaining for endothelial cells (factor VIII) is shown in early (*D*) and late generation (*E*) xenograft (*brown* color).

Envision+ System, HRP (anti-mouse K4006, anti-rabbit K4010; Dako, Glostrup, Denmark). Endogenous peroxidases were blocked with 0.03% hydrogen peroxide, and nonspecific binding was blocked with 2% fetal calf serum in 0.1% Triton X-100, Tris-buffered saline (T-TBS, pH 7.6). Sections were then incubated for 1 h at room temperature with primary antibodies (for Annexin A2, overnight incubation at 4 °C) followed by peroxidase-labeled polymer conjugate to anti-mouse or anti-rabbit immunoglobulins. After washing, sections were incubated for 5–20 min with the 3,3′-diaminobenzidine chromogen. For EGFR antibody, the staining was preceded by a demasking treatment: 5 min proteinase k (S3020; Dako) and 30 min retrieval solution (S1700; Dako) at 95 °C.

Primary Antibodies—The following primary antibodies were used: anti-von Willebrand factor/factor VIII, 1:400 (polyclonal rabbit, A0082, Dako); monoclonal mouse anti-Calnexin, 1:50 dilution (MAB3126, Clone C8.B6, Chemicon); monoclonal mouse anti-Annexin A2, 1:50 (610068, BD Biosciences); rabbit anti-Annexin A5, 1:200 (PA120A; Hyphen Biomed, Neuville-sur-Oise, France); monoclonal mouse anti-human EGFR, 1:50 (M7239, E30 Clone, Dako); and monoclonal mouse anti-human nestin, 1:200 (MAB5326, Chemicon). EGFR and nestin antibodies were human-specific. The nestin antibody was used as a control to identify tumor cells on the TMAs, allowing removal of the tumor-negative spots from the statistics.

FIG. 2. **Experimental work flow.** *A*, membrane fractions of tumor samples were obtained by ultracentrifugation on a sucrose step gradient (*B*). Light membranes (0.32–1.1 M sucrose) and plasma membranes (1.1–1.4 M) were used to compare protein expression in xenografts (derived from two patients (P6 and P17)) from early *versus* late generation rats. In addition protein expression profiles in plasma membranes were also studied over four consecutive xenograft generations in the two patients (iTRAQ3 for P6 and iTRAQ4 for P17). iTRAQ labeled peptide samples were separated in two dimensions of liquid chromatography (2D HPLC) and detected and quantified by MALDI-TOF/TOF. MS/MS spectra were searched against human and rat databases using GPS Explorer. Species-specific quantification was performed using special software. *C*, quality control for membrane protein enrichment is shown by immunoblot analysis for EGFR in homogenate (*H*), two wash-out fractions (*S1* and *S2*), light membranes (*LM*), and plasma membrane-enriched fractions (*PM*).
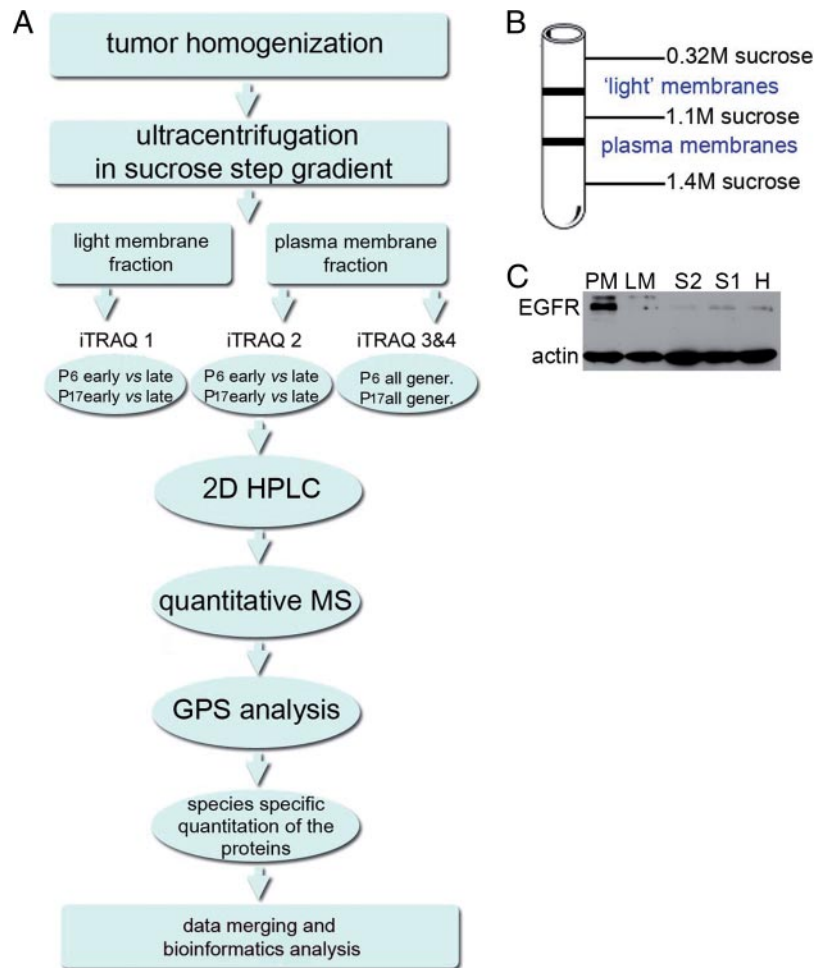
Tissue Microarrays

Xenograft TMA—The xenograft TMA was prepared from six generations of rat xenograft brain tumors derived from seven different GBM patients. A total of 20 early generation xenografts and 10 late generation tumors were spotted in triplicates. Five samples of normal rat brain were used as control.

Glioma TMA—A high density tissue microarray of primary gliomas and normal human brain tissue (GL208, US Biomax, Inc., Rockville, MD) was used. Tumor sections (5-μm thickness) of four grades were present in three replicates: astrocytoma grade 1 (eight patients), astrocytoma grade 2 (22 patients), astrocytoma grade 3 (16 patients), and glioblastoma multiforme (15 patients).

Staining—Endogenous peroxidase activity was blocked with 0.03% hydrogen peroxide, and nonspecific binding was blocked with 2% fetal calf serum in T-TBS, pH 7.6. The sections were then incubated for 1 h at room temperature with primary antibody. Immunohistochemical stainings were revealed using the Envision+ System, HRP (K4010, Dako). After washing, sections were incubated for 15 min with the 3,3′-diaminobenzidine chromogen.

TMA Quantification—For quantification of the immunostaining, all pictures were taken in the same background with a 50× magnification. The eight-bit pictures were analyzed with Image J software. The rolling ball algorithm was used to subtract the background, and the mean pixel intensity was determined on a normalized gray scale between 0 and 255. Values were visualized as box plots, and statistical analysis was done using the Mann-Whitney Wilcoxon rank test (*p* value ≤0.001).

Ingenuity Pathway Analysis

Functional analysis of the data set was done using the Ingenuity Pathway Knowledge Base (Ingenuity Systems, Redwood City, CA). The functional analysis identified biological functions and/or diseases that were most significant to the data set. Proteins showing highest expression in the angiogenic phenotype with a false discovery rate (FDR) of 30% (rank product list, supplemental Table 1) as well as proteins identified from the two major profiles from the trend data set over the four tumor generations (supplemental Table 2) were considered for the analysis. The analysis was done against the Ingenuity Pathway Knowledge Base. Fischer's exact test was used to calculate a *p* value determining the probability that each biological function and/or disease assigned to that data set is due to chance alone. Canonical pathway analysis identified the pathways from the Ingenuity Pathway Knowledge Base that were most significant to the data set. The significance of the association between the data set and the canonical pathways was measured 1) by the ratio of the number of proteins from the data set that map to the canonical pathway divided by the total number of proteins that map to the canonical pathway and 2) by Fisher's exact test (see above). The focus genes from the two short lists (supplemental Tables 1 and 2) were overlaid onto a global molecular network developed from information contained in the Ingenuity Pathway Knowledge Base. This generated networks based on the connectivity of the individual proteins.
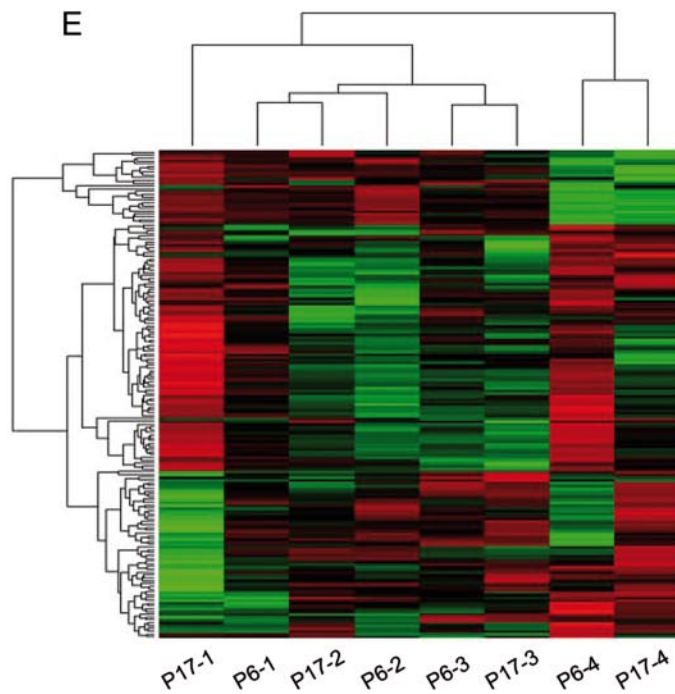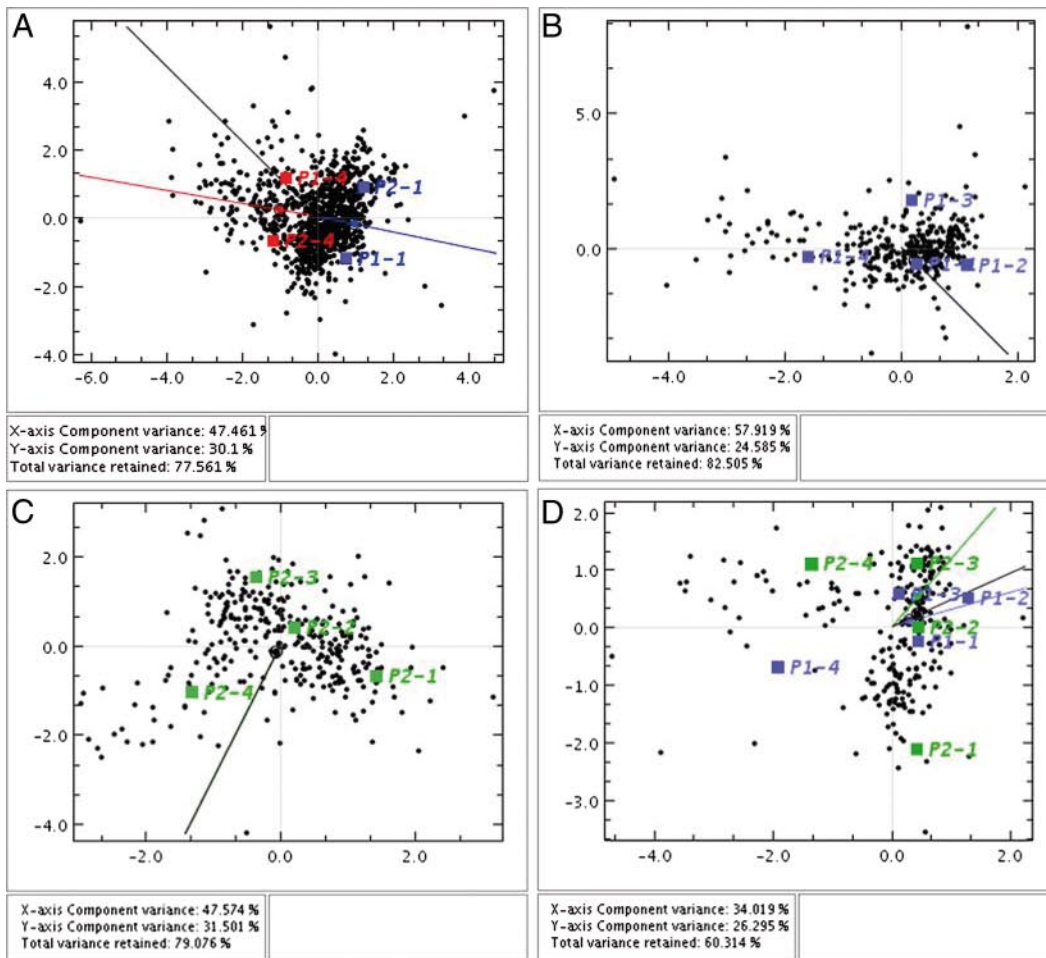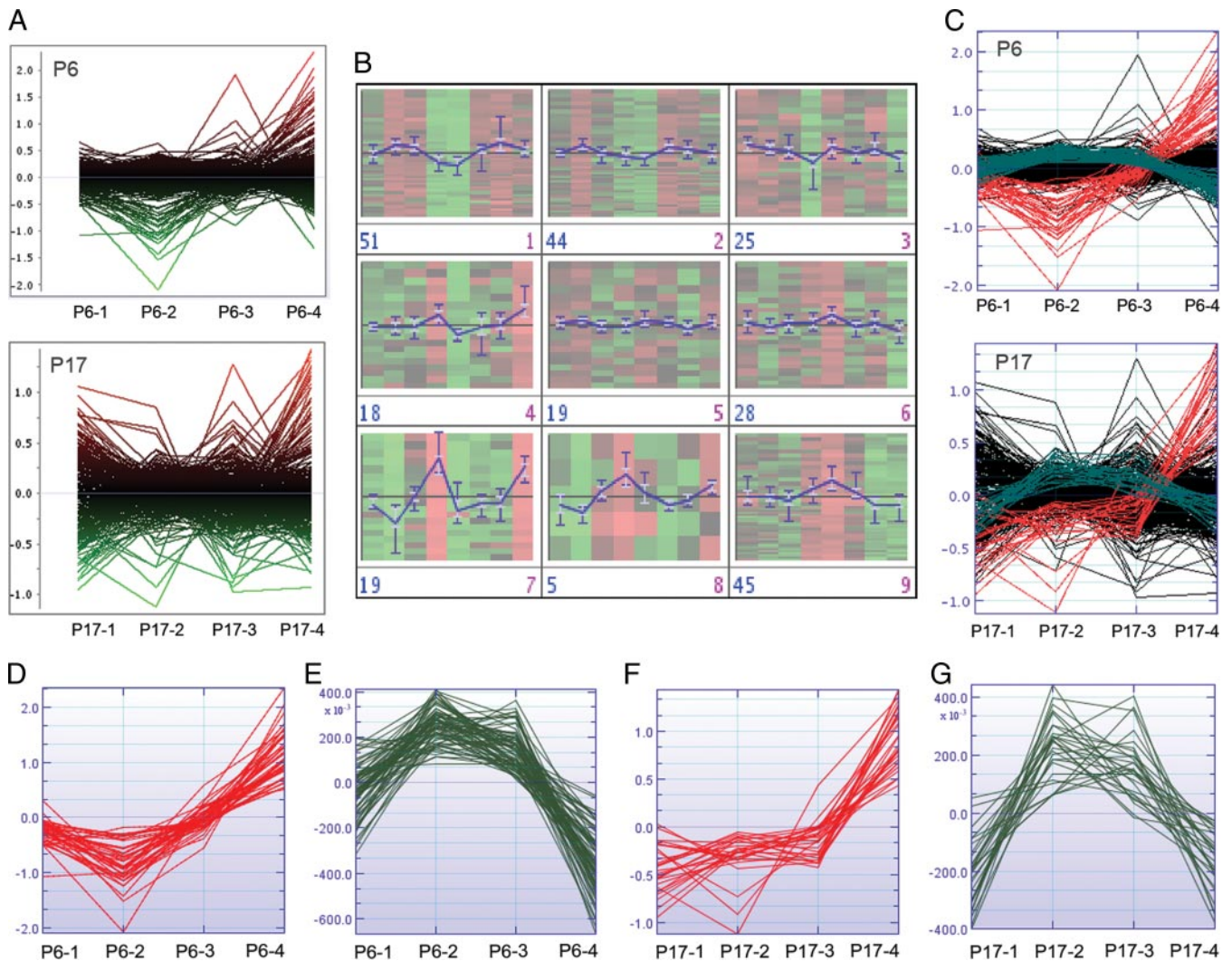
Fig. 4. **Unsupervised analysis of trend data sets.** *A*, proteins identified in tumor xenografts over four consecutive generations are plotted for P6 and P17. *B*, using self-organizing maps and profile searching, two consistent dominant profiles of protein expression were found in both patients (*C*). Profile I (*D* and *F*) shows proteins up-regulated in late/angiogenic tumors *versus* early/invasive tumors. These proteins are mainly of tumor/human origin. Profile II (*E* and *G*) shows the up-regulation of proteins in the two intermediary tumor generations. Proteins in this profile are mainly of host/rat origin. Note that not all proteins in the profiles are identical between P6 and P17. The *y axis* represents protein quantity value (log$_2$ intensity). P6-1, -2, -3, and -4 indicate the respective tumor generation derived from P6; idem for P17.

RESULTS

A Xenograft Model That Separates the Invasive and Angiogenic Compartment of Human GBM

We have previously generated an orthotopic rat xenograft model by transplantation of GBM tumor spheroids into the brain of immunodeficient rats (8, 23). Serial transplantation of tumor spheroids into consecutive generations of rats yields phenotypically distinct tumors with the most striking differences appearing between the early (first) and late (fourth to sixth) tumor generations (Fig. 1*A*). Early generation tumors are highly invasive, infiltrating the brain parenchyma and the contralateral hemisphere, but show little or no angiogenesis (Fig. 1, *B* and *D*). Late generation tumors are less invasive but show strong induction of neovascularization as determined on his-

Fig. 3. **Correspondence analysis plots and heat map.** *A*, the compiled data set of all proteins included for quantitative analysis comparing first generation (*blue*) and fourth generation (*red*) samples in P6 and P17. *B* and *C*, the four consecutive tumor generations derived from patient 6 (*B*) and from patient 17 (*C*). *D*, the combined data set of P6 (*blue*) and P17 (*green*) xenografts for 254 proteins overlapping in both experiments. *E*, a heat map of a global clustering of pairwise sample similarity. The best similarity was found in the late generation samples of the two patients (P17-4 and P6-4), and the biggest difference was found between early and late generations. *Rows* represent protein IDs; *columns* represent the different samples analyzed. P6-1, -2, -3, and -4 indicate the respective tumor generation derived from P6; idem for P17.

tological sections (Fig. 1, *C* and *E*) and on contrast enhanced magnetic resonance imaging indicating the presence of leaky blood vessels (8, 24). We have shown previously that the survival of rats with the infiltrative phenotype is between 120 and 150 days, whereas the survival of the angiogenic phenotype is between 40 and 60 days (8). Gene expression analysis revealed the up-regulation of genes related to angiogenesis including *VEGF*, *PDGFRA*, and *FGFR1* in the high generation tumors (8). With the progressive change from an invasive tumor growing by vessel co-option to an angiogenesis-dependent tumor phenotype, the animal model recapitulates the angiogenic switch observed in many solid tumors, including gliomas.

Species-specific iTRAQ Analysis of the Xenograft Brain Tumor Model

To identify membrane-associated proteins involved in the angiogenic switch we applied high throughput quantitative proteomics analysis on the xenograft tumor phenotypes. Isobaric peptide tagging coupled to LC and tandem MS was performed on membrane-enriched protein fractions of xenografted brain tumors derived from two different GBM patients (P6 and P17). Comparisons were done on samples from four generations of serially transplanted tumors and between first and late generation tumors (see Fig. 2 for experimental work flow). Membrane protein enrichment was confirmed by the accumulation in the plasma membrane fraction of EGFR, a tyrosine kinase receptor known to be up-regulated in a majority of human GBMs (Fig. 2*C*).

After protein digestion and peptide labeling, the samples were separated by two dimensions of LC: SCX columns (20 fractions) followed by reverse phase chromatography (192 fractions) yielding a total of 3840 fractions for each iTRAQ experiment that were spotted on MALDI plates and analyzed by mass spectrometry (a total of 15,360 spots for the four experiments). Over the four iTRAQ experiments this led to the identification of about 7500 redundant (non-unique) proteins (C.I. $\geq$ 95%) by GPS Explorer analysis in Swiss-Prot and NCBI rat and human databases. Taking advantage of the sequence dissimilarities between human and rat proteins, only peptides that could differentiate between the two species were considered in the subsequent analyses. Peptides with a sequence that did not discriminate between isoforms were also excluded resulting in about 3150 isoform- and species-specific proteins of which 1633 were of human/tumor origin and 1517 were of rat/host origin. This 1:1 ratio between human and rat IDs was constant throughout the data set, suggesting that there was no differential bias toward one or the other species in any of the samples. Of these, 1460 proteins were quantifiable based on identification with at least two peptides and a high annotation confidence (CI $\geq$ 95%), and 1038 thereof were present in both patients. Here again the distribution between human and rat remained similar (522 human, 511 rat).
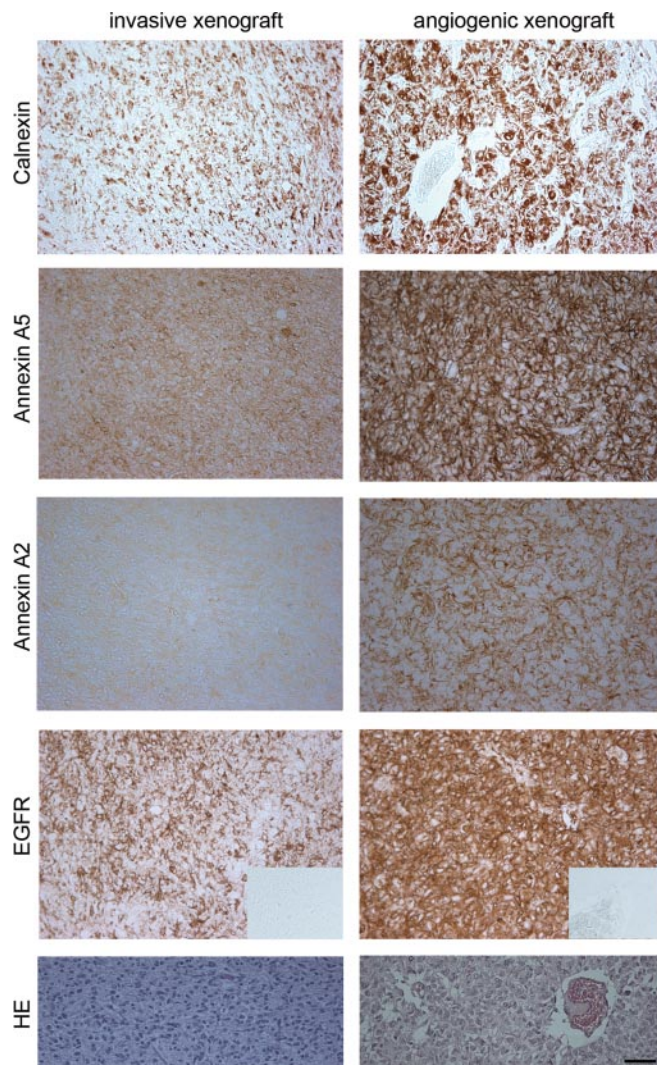

FIG. 5. **Validation of candidate proteins by immunohistochemistry.** Immunohistochemistry on paraffin-embedded sections of early and late generation tumors. Calnexin, AnxA2, and AnxA5 show increased expression in both late generation tumors (shown here for P17). EGFR is increased in angiogenic tumors of P6 only (shown here). *Insets* in the *EGFR panel* show an isotype control. The *lower panels* show a hematoxylin/eosin (*HE*) staining of a consecutive section for either invasive or angiogenic phenotype (*bar*, 50 μm).

Bioinformatics Analysis Identifies Different Protein Clusters between Invasive and Angiogenic Tumor Phenotypes

Correspondence Analysis—Using CA plots, global views of the different data sets were produced to reveal global relationships between the samples and between samples and proteins. Fig. 3*A* shows that the major global trend in the data set for analyzing differentially expressed proteins between early and late generations was indeed the separation of the two early and the two late generation samples along the first axis of the plot. Interestingly this effect was found to be larger in this estimated global view than the individual difference

FIG. 6. **Expression in xenograft tissue microarrays.** Immunohistochemistry and quantification thereof of candidate proteins Calnexin, AnxA5, AnxA2, and EGFR on TMAs of 20 early and 10 late generation xenograft tumors are shown. The *y axis* of the box plots corresponds to mean pixel intensity (relative units between 0 and 255). A highly significant increase in the expression of Calnexin and AnxA2 ($p \leq 0.001$) is observed in angiogenic phenotypes. AnxA5 is also up-regulated in angiogenic phenotypes but to a lesser extent ($p = 0.05$). No significant difference between xenograft phenotypes was detected for EGFR. As expected, human-specific nestin staining was also unchanged between the two phenotypes (*bar*, 50 μm). A representative core is shown *above* each quantification box plot. The *black bar* in the box indicates the median sample value; the *whiskers* indicate the *upper* and *lower* quartile, respectively. *Open circles* represent observations, which lie more than 1.5 times the interquartile range from the first and third quartile. *ctr br.*, control brain; *inv.*, invasive; *ang.*, angiogenic.
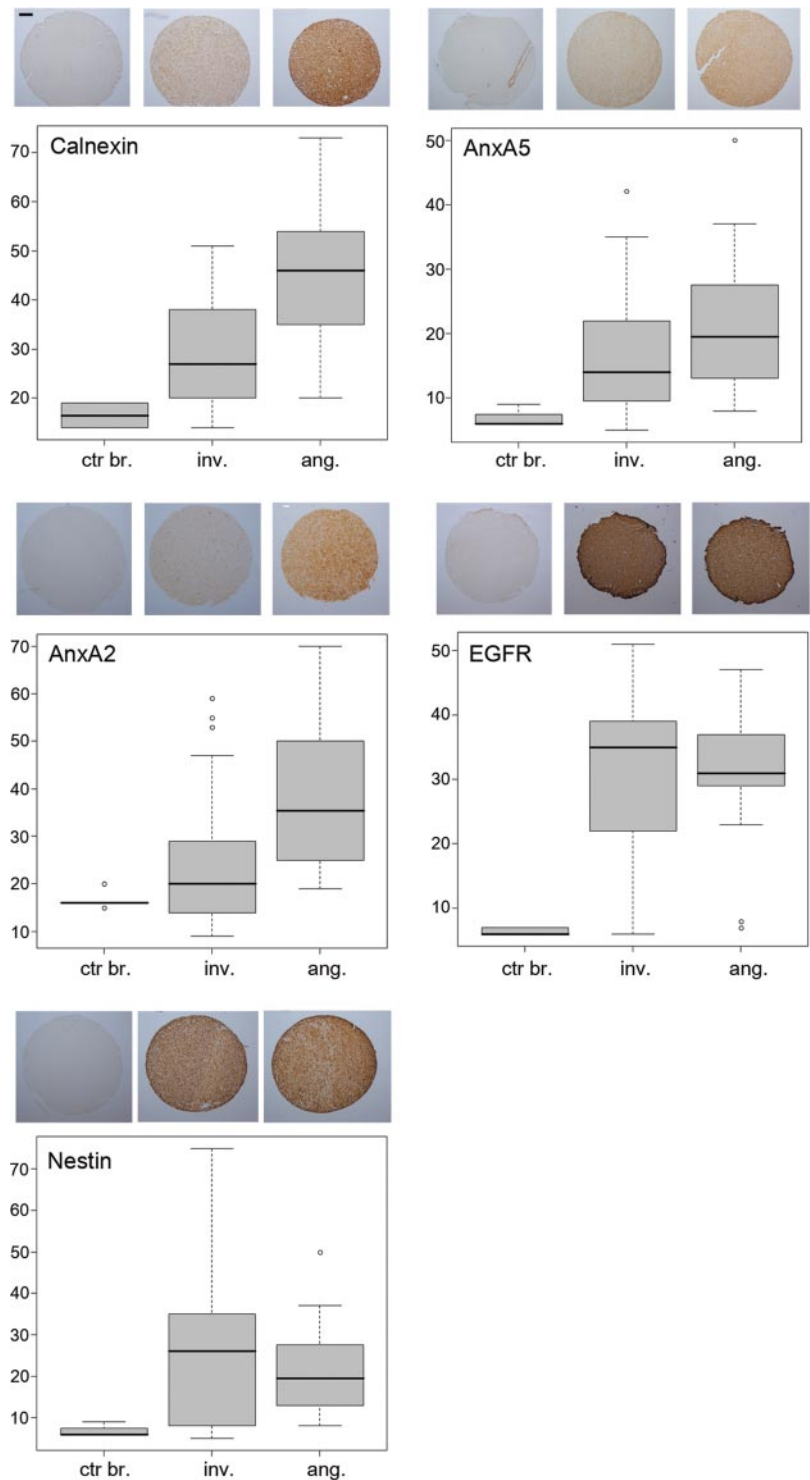
between P6 and P17, which was not even detected as the second largest major trend along the *y* axis. This suggests that the biological variation between human GBMs is less pronounced than the phenotypic variation observed between the different xenograft generations. Fig. 3*B* shows that the four consecutive tumor generations of P6 fall out in the plot in a sequential counterclockwise order around origo. The exact

same trend was seen for P17 (Fig. 3*C*). The similar trends of P6 and P17 were further confirmed by applying CA to only the proteins found to overlap in the P6 and P17 trend data sets (Fig. 3*D*). We then performed unsupervised cluster analysis to generate a heat map of a global clustering (Fig. 3*E*), describing "pairwise sample similarity." This again shows that the highest similarity was found between late generation tumors
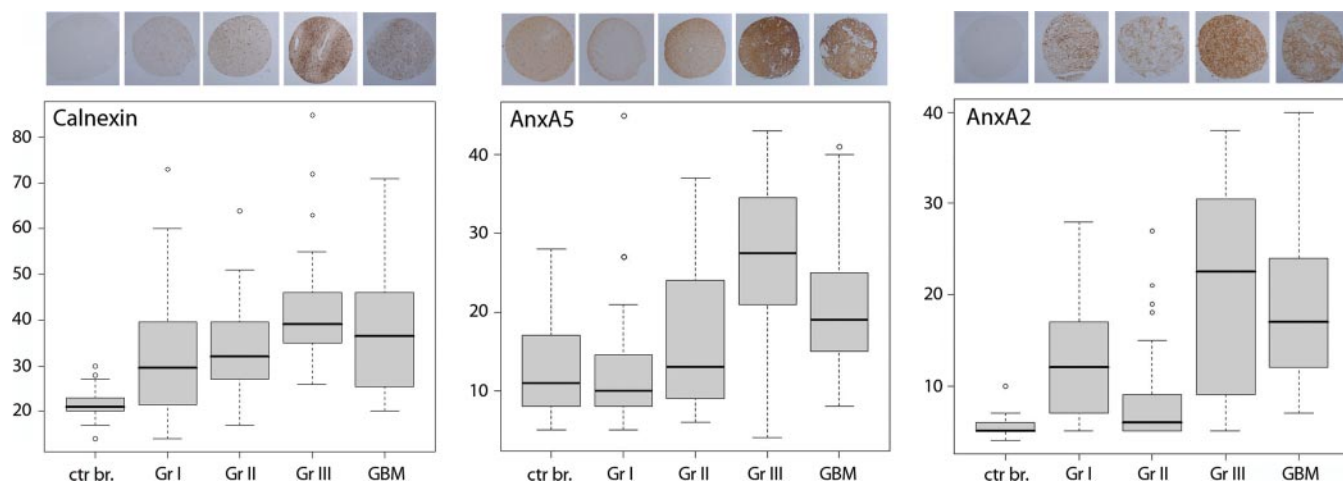
FIG. 7. **Expression in glioma tissue microarrays.** Immunohistochemistry and quantification thereof of candidate proteins Calnexin, AnxA5, and AnxA2 on a TMA containing more than 200 clinical gliomas (grades I–IV) are shown. The *y axis* of the box plots corresponds to mean pixel intensity (relative units between 0 and 255). A significant difference in expression was found between low grade (I and II) gliomas and high grade (III and IV) gliomas for Calnexin, AnxA5, and AnxA2 ($p < 0.001$). For AnxA2 a significant difference was also found between grade I and grade II. For AnxA5 the difference between grade II and grade IV was less significant ($p < 0.05$). All three proteins were expressed at a very low level in the normal human brain (*left bars*). A representative core is shown *above* each quantification box plot. The *black bar* in the box indicates the median sample value; the *whiskers* indicate the *upper* and *lower* quartile, respectively. *Open circles* represent observations, which lie more than 1.5 times the interquartile range from the first and third quartile. *ctr br.*, control brain; *Gr*, grade.

of the two patients (P17-4 and P6-4), and the biggest difference was between early and late generations (independent of patient). The CA plots and the heat map are indicative of the confidence of the data obtained as the observed sample clustering clearly reflects the histological similarities and dissimilarities of the tumor phenotypes.

Rank Product Analysis—The compiled data matrix for differential expression analysis between first and late generation xenografts had 1038 entries (only proteins overlapping in P6 and P17) representing 745 unique proteins. Using J-Express, the RankProduct algorithm (20) was applied to proteins identified in first and late generation tumors to find differentially expressed proteins consistent between the two biological replicates. This analysis provides *q* values to control for multiple testing, and at the level of about 30% FDR, proteins with the most significant up-regulation in the late generation were extracted (see supplemental Table 1 for expression values and protein IDs). The majority of the proteins up-regulated in the angiogenic phenotype were of human (tumor) origin. Despite the high FDR chosen here, many of these proteins were also extracted in the subsequent analysis comparing protein profiles over four tumor generations (see trend data set below).

Protein Profiles in Trend Data Sets—Next we analyzed the global plot of the two trend data sets over the four tumor generations derived from P6 and P17 (iTRAQ3 and iTRAQ4). Visual inspection clearly identified common dominant protein profiles that appear to be present in both data sets (Fig. 4*A*). By adjoining the data from P6 and P17 for shared proteins, proteins co-regulated in both patients can be detected by clustering. Using the self-organizing map clustering algorithm

these proteins were divided into nine clusters (Fig. 4*B*) from which two major common profiles were identified: the first one assembling proteins that were up-regulated in the late generation (derived from clusters 7, 8, and 4), and a second one showing peak protein expression in the middle generations (derived from clusters 1 and 2). Proteins with expression patterns similar to these global trends were extracted individually from the P6 and P17 data sets using Profile similarity search in J-Express, resulting in Profile I (*red*) and Profile II (*dark green*) highlighted for P6 and for P17 (Fig. 4*C*). Interestingly most proteins in the up-regulated Profile I were of human origin (Fig. 4, *D–G*). In P6 only one of 41 was of rat origin (Fig. 4*D*), and in P17 only one of 28 was of rat origin (Fig. 4*F*). The situation is exactly the opposite for Profile II where 48 of 70 proteins in P6 (Fig. 4*E*) and 26 of 28 in P17 (Fig. 4*G*) were of rat origin. The protein IDs and annotations from the profiles depicted in Fig. 4, *D–G*, are presented in supplemental Table 2.

Validation of Candidate Proteins by Immunostaining of Tissue Microarrays—Based on the rank product list (supplemental Table 1), we selected four proteins to validate their expression pattern by immunohistochemistry on a larger number of samples: Calnexin, Annexin A5 (AnxA5), and AnxA2, which showed a mean increase in angiogenic tumors of 3.7-, 3.4-, and 2.2-fold respectively (supplemental Table 1), and EGFR, which showed a mean increase of 2.2-fold but was only up-regulated in P6 and not in P17 (supplemental Table 1). The proteins were chosen throughout the rank product list to be representative of the top 60 proteins. Immunohistochemistry was performed on sections of the same xenograft tumors as those used for the iTRAQ analysis (derived from P6 and P17,

TABLE I

The main biological functions, networks, and diseases extracted from the rank product list and the associated protein IDs as assessed with Ingenuity Pathways Analysis

Proteins shown in italics were added to the networks by the Ingenuity Pathway Knowledge Base, which was used as a reference data set. MAPK, mitogen-activated protein kinase; ERK, extracellular signal-regulated kinase; PI3K, phosphatidylinositol 3-kinase; GAPDH, glyceraldehyde-3-phosphate dehydrogenase; Jnk, c-Jun NH$_2$-terminal kinase; PLC, phospholipase C.

Top functions	Associated molecules	Score	Focus molecules
Networks			
Cell-to-cell signaling and interaction, hematological disease, hematological system development and function	*Akt*, ALB, ANXA1, ANXA2, ANXA5, ANXA6, ATP1A2, *calmodulin*, *calpain*, CALR, CANX, CD9, CKAP4, COX2, CYCS (includes EG:54205), EGFR, *ERK*, *F-actin*, GAP43, GAPDH (includes EG:2597), HSPD1, *interferon α*, *Jnk*, *Mapk*, MARCKS (includes EG:4082), MARCKSL1, *MHC class I*, *NFκB*, *p38 MAPK*, P4HB, PDIA3, *PI3K*, *Pkc(s)*, *PLC*, *Ras*	47	20
Amino acid metabolism, small molecule biochemistry, lipid metabolism	*Acetyl-CoA C-acetyltransferase*, ASGR1, *ATF4*, CPT2, *CS*, *CYC1*, *cytochrome bc₁*, *FH*, GANAB, GOLIM4, *GOT2*, HADHA, HADHB, *HLA-F*, *HNF4A*, HSPA9, *IFNB1*, *KARS*, KRT2, LETM1, *MAGEA1 (includes EG:4100)*, MDH2, *NFKB1*, *PELO*, PYCR1, *SGK1*, SLC25A6, *SMAD3*, SSBP1, *TIMM23*, TIMM50, UQCRB, UQCRFS1, *UQCRFSL1*, *UQCRH*	32	15
Energy production, nucleic acid metabolism, small molecule biochemistry	*Adenosine-tetraphosphatase*, AGT, *ATP5A1*, *ATP5B*, *ATP5C1*, *ATP5D*, *ATP5E*, ATP5F1, ATP5L, *ATP6V0C*, *β-estradiol*, *CR1*, *CRABP2*, CRIP2, *cyclic GMP*, DECR1, *FDFT1*, *H⁺-transporting two-sector ATPase*, *hemin*, *HLA-DRB1*, IDH2, *IFNG*, MARCKSL1, *MSR1*, *NFYA*, PDIA3, *PHLDA3*, PKM2, *PLA2G1B*, RRBP1, SDHA, SLC1A3, *TAP2*, TOMM22	27	13

Top functions	Associated molecules	*p* value	No. of molecules
Diseases and disorders			
Neurological disease	ANXA2, ATP1A2, ATP5A1, ATP5L, CALR, CANX, COX2, CYCS (includes EG:54205), EGFR, GAP43, GAPDH (includes EG:2597), HADHA, HADHB, HSPD1, MARCKS (includes EG:4082), MARCKSL1, PDIA3, PKM2, SDHA, SLC1A3, SLC25A6, SSBP1, UQCRB	2.43e−07–4.87e−02	24
Cancer	ALB, ANXA1, ANXA2, PKM2, CD9, EGFR, CALR, COX2, ANXA5, ATP1A2, CANX, P4HB, GAP43, SLC25A6, CYCS (includes EG:54205), GAPDH (includes EG:2597), HSPD1, PDIA3, DECR1, SLC1A3	5.32e−06–4.98e−02	20
Molecular and cellular functions			
Energy production	ATP1A2, ATP5A1, ATP5F1, ATP5L, MDH2, HSPD1, CYCS (includes EG:54205), SDHA, UQCRFS1	2.32e−06–2.64E−02	9
Nucleic acid metabolism	ATP1A2, ATP5A1, ATP5F1, ATP5L, HADHA, HSPD1, EGFR, GAPDH (includes EG:2597), CYCS (includes EG:54205)	2.32e−02–2.47e−02	9
Small molecule biochemistry	HSPD1, CALR, P4HB, MDH2, CYCS (includes EG:54205), ATP1A2, MARCKS (includes EG:4082), GANAB, HADHB, SLC1A3, EGFR, ANXA2, ANXA5, PDIA3, CD9, ATP5A1, HADHA, ATP5F1, ATP5L, ALB, PYCR1, GAPDH (includes EG:2597), CPT2, ANXA1	2.32e−06–4.53e−02	24
Cell-to-cell signaling and interaction	HSPD1, CALR, EGFR, ANXA2, ANXA5, CKAP4, KRT2, PDIA3, MARCKSL1, GAP43, CD9, ALB, ANXA1	1.24e−05–4.98e−02	13

TABLE I—*continued*

Top functions	Associated molecules	*p* value	No. of molecules
Molecular transport	CALR, ATP1A2, MARCKS (includes EG:4082), SLC1A3, UQCRFS1, CCHCR1, SDHA, PDIA3, CD9, HADHA, ALB, ANXA1, HSPA9, CPT2, GAPDH (includes EG:2597)	$2.77e-05–4.53e-02$	15

Top functions	Associated molecules	*p* value	Ratio
Canonical pathways			
Oxidative phosphorylation	ATP5A1, ATP5F1, ATP5L, COX2, SDHA, UQCRB, UQCRFS1	$5.62e-07$	7:157
Mitochondrial dysfunction	ATP5A1, COX2, CYCS (includes EG:54205), SDHA, UQCRB, UQCRFS1	$1.52e-05$	6:170

respectively). The differential expression was confirmed for all four proteins on the original xenograft material (Fig. 5). Next we performed immunostaining for the four proteins on TMAs of early and late generation xenografts of additional GBMs. In confirmation of the iTRAQ data, Calnexin, AnxA5, and AnxA2 showed increased expression in angiogenic compared with invasive tumors in the xenografts of the TMA slide (Fig. 6). Quantification of the staining intensity demonstrated a highly significant ($p < 0.001$, Wilcoxon rank test) increase in protein expression for Calnexin (1.6-fold) and AnxA2 (1.5-fold) and a 1.3-fold increase of AnxA5 (at the border of significance, $p = 0.05$) (Fig. 6). TMA analysis showed that EGFR expression was high in most xenograft samples independent of tumor phenotype. However, a high variability was observed between different xenografts presumably reflecting the known cellular variability of EGFR expression in human GBMs. Quantification of EGFR staining showed no significant difference between invasive and angiogenic xenografts (Fig. 6), suggesting that when EGFR is overexpressed in the original GBM its expression level is retained in the animal model independently of the phenotype. It should be noted, however, that differences in specific isoforms of EGFR cannot be excluded because the antibody used here does not discriminate between wild type and EGFR mutants (*e.g.* the truncated EGFRvIII mutant). Human-specific nestin staining, labeling the vast majority of GBM cells, was used as a control to detect human cells on the xenograft TMA. As expected its expression was not changed between early and late generation xenografts (Fig. 6). In summary, from the rank product list four selected proteins were validated on the original xenograft material as well as on a large number of GBM xenografts.

We further evaluated the expression of Calnexin, AnxA5, and AnxA2 in patient specimens of different glioma types (grades I to IV) using a TMA containing about 180 clinical cores (Fig. 7). Interestingly all three proteins showed increased expression in high grade (III and IV) compared with low grade (I and II) gliomas. The difference in expression was highly significant ($p < 0.001$) and was particularly pronounced for AnxA2 (Fig. 7). These data suggest that Calnexin, AnxA2,

and AnxA5 may be further exploited as biomarkers for malignant glioma.

Increase in Cellular Cross-talk and Oxidative Metabolism in Angiogenic Genotype

Gene Ontology (GO) Classification—To get an overall idea of the type of proteins identified in the present screen, we applied the GO annotation tool in the J-Express software to the total set of 745 unique proteins overlapping between P6 and P17. Of these, 322 belonged to the GO class "cellular component" of which a majority mapped to the terms membrane (182), intracellular organelle (146), mitochondrion (102), and endoplasmic reticulum and Golgi (42). Only 48 mapped to the term cytosol, indicating that the majority of proteins identified indeed correspond to plasma and organelle membrane-associated proteins, confirming the robustness of the prefractionation protocol.

Functional Analysis of Data Sets—To further interpret our findings in a biological context, the top 60 proteins from the rank product list (supplemental Table 1) and the proteins from the two main profile lists (supplemental Table 2) were analyzed through the Ingenuity Pathway Knowledge Base. This functional analysis identifies biological functions and/or diseases that are most significant to the data set. The rank product list, representing proteins up-regulated in the angiogenic phenotype, generated the following top networks: (i) cell-to-cell signaling and interaction (score, 47), (ii) amino acid and lipid metabolism (score, 32), and (iii) energy production/nucleic acid metabolism (score, 27). The proteins attributed to the networks are shown in Table I. Neurological disease and cancer were the main diseases connected to the list. The top canonical pathways associated with high significance were oxidative phosphorylation and mitochondrial dysfunction (see Table I for protein IDs and associated *p* values). Next we analyzed the proteins from the two major profiles from the trend data set (Fig. 4) that are of particular interest as they reveal differences between host and tumor responses. Profile I from the trend data set (supplemental Table 2), consisting largely of tumor proteins found to be increased in the angio-

TABLE II

The main biological functions, networks, and diseases extracted from profile I and their associated protein IDs as assessed with Ingenuity Pathways Analysis

Proteins shown in italics were added to the networks by the Ingenuity Pathway Knowledge Base, which was used as a reference data set. MAPK, mitogen-activated protein kinase; ERK, extracellular signal-regulated kinase; Jnk, c-Jun NH_2-terminal kinase; PLC, phospholipase C; LDL, low density lipoprotein; PDGF, platelet-derived growth factor; FSH, follicle-stimulating hormone.

Top functions	Associated molecules	Score	Focus molecules
Networks			
Lipid metabolism, small molecule biochemistry, cancer	ACAT1, *acetyl-CoA C-acetyltransferase*, ANXA5, ANXA6, COX2, COX4I1, COX7A2, CS, CTNND1, CYCS (includes EG:54205), *cytochrome c oxidase*, EGFR, *ERK*, HADHA, HADHB, *Hsp90*, HSP90B1, HSPA9, HSPD1, *insulin*, *interferon α*, *Jnk*, *LDL*, MDH2, NDUFB9, *NFκB*, *p38 MAPK*, *PDGF BB*, PDIA3, *Pkc(s)*, *PLC*, *Ras*, SLC25A11, UQCRC1, UQCRFS1	49	21
Cancer, cardiovascular disease, cell morphology	ACO2, ALDH6A1, ANXA3, *β-estradiol*, *C11ORF10*, *C9ORF5*, CDC123, CECR5, CHCHD3, *CHCHD8*, *CPA2*, DECR1, DLST, *GINS3*, *HNF4A*, *HRAS*, IDH2, KRT2, KRT10, *LOC284230*, *MINA*, *MYC*, NFKB2, *OAS1H*, *OLFR1508*, RPL31, *RPL21 (includes EG:79449)*, RRBP1, *RSPH3*, SDHA, SFXN1, *SIN3A*, *SMAD3*, *TERT*, TIMM50	32	15
Energy production, nucleic acid metabolism, small molecule biochemistry	*Adenosine-tetraphosphatase*, ALDOA, AQP4, ATP5A1, *ATP5B*, ATP5F1, *ATP5H (includes EG:10476)*, *ATP5H (includes EG:641434)*, ATP5L, ATP5O, *ATP5S*, *ATP6AP1*, *ATP6V0A2*, *ATP6V0E2*, *ATP6V1C1*, *ATP6V1C2*, *ATP6V1E2*, *ATP6V1G3*, C21ORF33, CALD1, *calmodulin*, *Ck2*, CKAP4, *F-actin*, *FSH*, H^+-*transporting two-sector ATPase*, *histone h3*, *Mapk*, MARCKS (includes EG:4082), PKM2, *PPP2R2B*, SEPT11, TOMM22, *TRAF6*, TUFM	29	14

Top functions	Associated molecules	p value	No. of molecules
Diseases and disorders			
Genetic disorder	HSPD1, AQP4, PKM2, HADHB, RPL31, UQCRFS1, EGFR, ATP5O, CALD1, SDHA, KRT2, TUFM, ALDH6A1, HSP90B1, ATP5A1, ATP5L, KRT10, CYCS (includes EG:54205), ALDOA, MARCKS (includes EG:4082), COX2, ACAT1, PDIA3, COX7A2, HADHA, UQCRC1, C14ORF2	$5.68e-06–4.62e-02$	27
Neurological disease	HSPD1, KRT10, CYCS (includes EG:54205), MARCKS (includes EG:4082), AQP4, PKM2, RPL31, HADHB, EGFR, COX2, ATP5O, SDHA, ACAT1, PDIA3, TUFM, ALDH6A1, HSP90B1, COX7A2, ATP5A1, HADHA, UQCRC1, ATP5L, C14ORF2	$4.05e-07–4.98e-02$	23
Hematological disease	PDIA3, HSP90B1, ALDOA, ANXA6, HADHA, ANXA3, ACO2, EGFR, ANXA5, CALD1	$1.55e-06–4.98e-02$	10
Molecular and cellular functions			
Energy production	HSPD1, CYCS (includes EG:54205), MDH2, COX4I1, ACO2, UQCRFS1, ATP5O, DLST, SDHA, ATP5A1, ATP5F1, ATP5L, UQCRC1	$2.53e-06–2.52e-02$	13
Small molecule biochemistry	HSPD1, CYCS (includes EG:54205), MDH2, MARCKS (includes EG:4082), HADHB, ACO2, EGFR, ATP5O, ANXA5, ACAT1, PDIA3, ALDH6A1, ATP5A1, HADHA, ATP5F1, ATP5L	$2.53e-06–3.93e-02$	16
Cell death	DLST, HSPD1, KRT10, CYCS (includes EG:54205), HSP90B1, HADHA, DECR1, EGFR, COX2, HSPA9, ANXA5	$1.03e-03–4.98e-02$	11

Top functions	Associated molecules	*p* value	Ratio
Canonical pathways			
Oxidative phosphorylation	SDHA, COX7A2, ATP5A1, COX4I1, NDUFB9, ATP5F1, UQCRFS1, ATP5L, UQCRC1, COX2, ATP5O	1.98e−12	11:157
Mitochondrial dysfunction	SDHA, CYCS (includes EG:54205), COX7A2, ATP5A1, COX4I1, NDUFB9, UQCRFS1, UQCRC1, COX2	3.13e−09	9:170
Citrate cycle	DLST, SDHA, MDH2, IDH2, CS, ACO2	5.60e−06	6:59

genic phenotype, generated the following major networks: (i) lipid metabolism/small molecule biochemistry (score, 49), (ii) cancer/cell morphology (score, 32), and (iii) energy production/nucleic acid metabolism (score, 29). The major diseases associated to this data set are genetic disorder and neurological disease. The top canonical pathways identified with high significance are oxidative phosphorylation and mitochondrial dysfunction. The proteins attributed to the networks, diseases, and canonical pathways are shown in Table II. Profile II from the trend data set (supplemental Table 2), consisting largely of host-derived (rat) proteins that showed slightly increased expression in the intermediate generations, generated the following major networks: (i) cellular function and maintenance (score, 68), (ii) energy production/lipid metabolism (score, 36), and (iii) energy production/nucleic acid metabolism (score, 34). The major diseases associated with this data set are again genetic disorder and neurological disease. The top canonical pathways identified with high significance are oxidative phosphorylation and mitochondrial dysfunction. The proteins attributed to these networks, diseases, and canonical pathways are shown in Table III.

DISCUSSION

In the present study we applied isobaric peptide tags (iTRAQ) and multidimensional LC-MS/MS to identify proteins that are differentially expressed in invasive compared with angiogenic brain tumor specimens derived from an orthotopic xenograft model that recapitulates the angiogenic switch. We have earlier shown that this model maintains key biological features of human GBMs *in situ* (8, 24). Although it is presently not clear whether the phenotypic shift observed after serial passaging is due to a selection process or an increased adaptation of the tumor cells to the host microenvironment, the resulting tumor phenotype closely recapitulates the major clinical features of human GBM, including glioma cell heterogeneity, mutational profile, and invasive and angiogenic properties. Aiming at the identification of novel biomarkers and potential molecular targets for malignant gliomas, we focused on profiling the membrane-enriched subproteome.

The combination of subfractionation, iTRAQ-based labeling, 2D LC peptide separation, and MALDI-TOF/TOF mass spectrometry connected to database searches for human and rat proteins yielded several thousand protein IDs over four iTRAQ experiments. Taking advantage of the xenograft model, we focused on those proteins that were extracted as isoform- and species-specific based on their sequence identity, thus ensuring that the origin of the proteins (tumor- or host-derived) was unequivocal. Interestingly the number of human protein IDs was very similar to the number of rat IDs, suggesting that there was no bias in species contribution between different samples. Only proteins identified with at least two peptides/protein and a high annotation confidence (≥95%) were considered, resulting in 1460 quantifiable proteins over the four experiments. Correspondence analysis and heat map plots revealed a high degree of similarity between tumor xenografts of the same generation although arising from different patient GBMs. This indicates that the xenograft animal model provides reproducible tumor specimens derived from different patients. It is also a strong indication of the validity of the overall data set because it clearly mirrors the histological findings. This is of major importance for studies with rare, clinical material and for this study in particular where the elaborate and time-consuming establishment of the animal model restricted the number of available GBM tumor xenografts. A similar trend was seen in the analysis of the trend data set comparing the expression profiles over four consecutive tumor generations. Here again the two major profiles extracted were identical between the two patients. The first most abundant profile encompasses the proteins that showed increased expression in the angiogenic, late generation tumor phenotype. Proteins from the second major profile showed a slightly increased expression in the second and third generation tumors (with intermediate phenotype) and dropped down in the late generation, angiogenic phenotype. Interestingly the large majority of proteins from Profile I were of human origin (tumor proteins), whereas those from Profile II were largely host-derived (rat proteins). The fact that the overall distribution of rat *versus* human IDs was 1:1 suggests that the species-specific protein regulation in these subsets is significant.

Obviously species- and isoform-specific quantification was achieved at the expense of the number of included peptides. In fact 76% of unique peptides were discarded in the present analysis focusing on *species*- and *isoform*-specific proteins. However, these peptides may provide important additional information and will be used to further validate the current data. This is currently under investigation, in particular taking into account the comparison with a gene expression study carried out on the same tumor samples.[2]

---

[2] K. Petersen and S. P. Niclou, unpublished data.

TABLE III

The main biological functions, networks, and diseases extracted from profile II and their associated protein IDs as assessed with Ingenuity Pathways Analysis

Proteins shown in italics were added to the networks by the Ingenuity Pathway Knowledge Base, which was used as a reference data set. ERK, extracellular signal-regulated kinase.

Top functions	Associated molecules	Score	Focus molecules
Networks			
Cellular function and maintenance, genetic disorder, neurological disease	ACAT1, CS, *cytochrome bc₁*, *ERK*, GOT2, HK1, *insulin*, *malate dehydrogenase*, MDH2, MFN2, *NADH2 dehydrogenase*, ND1, NDUFA5, NDUFA6, NDUFA12, NDUFA10 (includes EG: 4705), NDUFA9 (includes EG:4704), NDUFS1, NDUFS2, NDUFS3, NDUFS4, NDUFS8, NDUFV3 (includes EG:4731), PC, SLC25A4, SLC25A11, SLC25A12, SOD2, *Ubiquinol-cytochrome-c reductase*, UQCRC1, UQCRC2, UQCRFS1, UQCRQ, VDAC1, VDAC2	68	29
Energy production, lipid metabolism, small molecule biochemistry	ACO2, ACSL6, CEND1, *COX11*, *COX15*, *COX10 (includes EG:1352)*, COX4I1, *COX4I2*, COX5B, COX6B1, *COX6B2*, COX6C, COX7A2, *COX7B*, *COX7B2 (includes EG:170712)*, COX7C (includes EG:1350), *COX8A*, *COX8B*, *COX8C*, CPT1A, *cytochrome c oxidase*, FXC1, *HNF4A*, IDH3B, MTX1 (includes EG:4580), *NRF1*, *oleic acid*, PRDX3, *PRMT1*, SDHA, SFXN1, SUCLA2, SUCLG1, *TMBIM4*, *YY1*	36	18
Energy production, nucleic acid metabolism, small molecule biochemistry	*Adenosine-tetraphosphatase*, ATP8, *ATP5B*, ATP5C1, ATP5F1, ATP5H (includes EG:10476), *ATP5H (includes EG:641434)*, ATP5I, ATP5J, ATP5O, *ATP5S*, *ATP6AP1*, *ATP6V0E2*, *ATP6V1C2*, *ATP6V1E2*, BDH1, CIT, *cyclic AMP*, DLAT, GRM2, *H⁺-transporting two-sector ATPase*, LONP1, *NADH*, *NADH dehydrogenase*, *NADH2 dehydrogenase (ubiquinone)*, ND5, *NDUFA4L*, NDUFV1, PDHA1 (includes EG:5160), PDHB, *PDPK1*, *Ras*, *Ras homolog*, SYNGAP1, TOMM70A	34	18

Top functions	Associated molecules	*p* value	No. of molecules
Diseases and disorders			
Genetic disorder	HSPD1, SUCLA2, COX6C, CIT, ATP5J, UQCRFS1, UQCRC2, ATP5O, VDAC1, CPT1A, NDUFS4, SDHA, GRM2, VDAC2, NDUFS2, SMPD3, NDUFS3, COX5B, ATP5H (includes EG:10476), SLC25A4, SLC25A22, SLC25A3, COX7C (includes EG:1350), PLEC1, SHANK3, ATP5C1, MFN2, NEFM, PC, NDUFS8, AUH, UQCRQ, GPX4, ACAT1, NDUFS1, NDUFA5, SOD2, COX7A2, SUCLG1, PDHA1 (includes EG:5160), NDUFV1, UQCRC1, THY1	$5.55e{-}11$–$3.83e{-}02$	43
Neurological disease	HSPD1, SUCLA2, COX6C, CIT, ATP5J, UQCRC2, ATP5O, VDAC1, CPT1A, NDUFS4, SDHA, GRM2, VDAC2, NDUFS2, NDUFS3, COX5B, ATP5H (includes EG:10476), SLC25A4, SLC25A22, COX7C (includes EG:1350), ATP5C1, NEFM, MFN2, NDUFS8, UQCRQ, GPX4, ACAT1, NDUFA5, COX7A2, SOD2, PDHA1 (includes EG:5160), NDUFV1, UQCRC1, THY1	$5.55e{-}11$–$4.46e{-}02$	34

TABLE III—*continued*

Top functions	Associated molecules	*p* value	No. of molecules
Molecular and cellular functions			
Cellular function and maintenance	HSPD1, SYNGAP1, NDUFS4, MFN2, NDUFS1, NEFM, SOD2, HK1, SLC25A12, UQCRC1, UQCRC2, VDAC1	$1.39e-08$–$4.46e-02$	12
Energy production	HSPD1, COX7C (includes EG:1350), ATP5C1, ATP5I, MDH2, PC, COX4I1, COX6C, ATP5J, UQCRFS1, ACO2, ATP5O, GPX4, SDHA, NDUFS1, ATP5F1, UQCRC1, SLC25A4, SLC25A3	$1.64e-08$–$2.57e-02$	19
Small molecule biochemistry	HSPD1, MDH2, ATP5J, ACO2, IDH3B, ATP5O, VDAC1, CPT1A, GOT2, DLAT, ECHS1, SMPD3, ATP5F1, PRDX3, SLC25A4, SLC25A22, C1QBP, ATP5C1, ND1, ATP5I, ACSL6, MFN2, SLC25A12, GPX4, ACAT1, NDUFS1, SOD2, PDHB	$1.64e-08$–$4.46e-02$	28

Top functions	Associated molecules	*p* value	Ratio
Canonical pathways			
Oxidative phosphorylation	NDUFA10 (includes EG:4705), COX4I1, COX6C, ATP5J, ATP8, UQCRFS1, UQCRC2, ATP5O, SDHA, NDUFS4, COX6B1, NDUFA12, NDUFS2, NDUFS3, COX5B, NDUFV3 (includes EG:4731), ATP5H (includes EG:10476), ATP5F1, ND5, COX7C (includes EG:1350), ATP5I, ND1, ATP5C1, NDUFS8, UQCRQ, NDUFA6, NDUFA5, NDUFS1, COX7A2, NDUFA9 (includes EG:4704), NDUFV1, UQCRC1	$1.65e-40$	32:157
Mitochondrial dysfunction	NDUFA10 (includes EG:4705), CYB5R3, COX4I1, COX6C, ATP5J, UQCRFS1, UQCRC2, CPT1A, NDUFS4, SDHA, COX6B1, NDUFA12, NDUFS2, NDUFS3, NDUFV3 (includes EG:4731), COX5B, PRDX3, ND5, COX7C (includes EG:1350), ATP5C1, NDUFS8, NDUFA6, GPX4, NDUFS1, NDUFA5, SOD2, COX7A2, NDUFA9 (includes EG:4704), PDHA1 (includes EG:5160), NDUFV1, UQCRC1	$2.73e-39$	31:170
Ubiquinone biosynthesis	NDUFA10 (includes EG:4705), ND1, NDUFS8, NDUFA6, NDUFS4, NDUFS1, NDUFA5, NDUFA12, NDUFA9 (includes EG:4704), NDUFS2, NDUFV3 (includes EG:4731), NDUFV1, NDUFS3, ND5	$8.52e-18$	14:104

The expression pattern of Calnexin, AnxA2, AnxA5, and EGFR was confirmed by immunostaining on tissue microarrays of a large number of invasive and angiogenic xenografts as well as on glioma TMAs. The proteins were chosen from the rank product list on the basis of (*a*) their strong regulation (Calnexin), (*b*) the representation of a protein family (Annexins), or (*c*) their known role in GBM biology (EGFR). The validation of the iTRAQ result for all four proteins suggests that the combined proteomics and bioinformatics analysis applied has generated valid candidates that may be further evaluated for their role in the progression from invasive to angiogenic brain tumors. Obviously the validation of a handful of proteins cannot be extrapolated to the full protein list.

Calnexin is a calcium-binding, endoplasmic reticulum-associated protein that is involved in protein folding and assembly as well as the quality control of protein folding (25). It has an additional function in the assembly of MHC class I proteins as part of the antigen processing machinery (26), which plays a crucial role in the interaction between malignant cells and the immune system of the host. Calnexin is highly expressed in many human cancers, but an up-regulation in malignant gliomas has not been reported previously. Its functional role in angiogenesis and glioma progression remains to be addressed.

Annexins belong to a large family of calcium-dependent phospholipid-binding molecules with Annexin repeats, which are involved in several cellular processes including cell growth, signal transduction, apoptosis, inflammation, and differentiation. In addition to AnxA2 and AnxA5, the present screen identified Annexins A1, A3, and A6, all of which

showed increased expression in the angiogenic tumors. AnxA3, one of the proteins that was increased in the host compartment of angiogenic tumors, is known to promote endothelial cell migration and proliferation possibly via induced VEGF production (27). Interestingly AnxA3 has recently been identified in two proteomics screens in the injured central nervous system with its expression being limited to activated microglia (28, 29). The cellular origin of AnxA3 in our brain tumor model has not been investigated yet, but the fact that it is host-derived may point to microglial production, suggesting that activated microglia in malignant glioma contribute to tumor angiogenesis.

AnxA2 is classified as a candidate cancer marker (protein atlas), and its expression in gliomas correlates with malignancy (30). Indeed we confirmed increased expression of AnxA2 in grade III and IV gliomas on a large glioma TMA, suggesting that AnxA2 may be a novel biomarker for malignant gliomas. It has an important role in neoangiogenesis during development (31) and is involved in tumor angiogenesis presumably through its role in plasmin and metalloproteinase activation, which leads to increased VEGF production (32, 33). It has therefore been proposed as a potential antiangiogenic cancer target (32). Clearly the Annexin protein family deserves further attention with regard to glioma angiogenesis and progression.

GBM frequently involves amplification and alteration of the EGFR gene, resulting in overexpression of wild type and/or mutated forms of the receptor, including the most common mutation, EGFRvIII (34). EGFR gene status and expression is a negative prognostic factor for patients with GBM, especially in younger patients (35). EGFR signaling promotes proliferation, migration, and invasion and inhibits glioma cell apoptosis (36). In our xenograft model, the expression of this receptor appears to be independent of the tumor phenotype but is likely linked to the original patient biopsy from which the xenograft was derived. This supports the notion that the genetic mutations (in this case EGFR amplification) are maintained in our xenograft model.

Although the bioinformatics and functional analysis should be considered as hypothesis-generating, important trends can be identified in the data set. GO annotations and initial functional pathway analysis revealed that many proteins with increased expression in angiogenic tumors are associated with metabolic processes (energy production and lipid and nucleic acid metabolism) as well as cell-to-cell signaling and interaction. The data suggest that the angiogenic phenotype is characterized by an aerobic metabolism for energy production (oxidative phosphorylation) and a more active general cellular metabolism compared with the non-angiogenic phenotype. The canonical pathway of mitochondrial dysfunction suggests that alternative metabolic pathways may additionally be recruited in tumor cells for efficient energy production. These data are consistent with the higher growth rate of the angiogenic tumors. Conversely the infiltrative, non-angiogenic

tumor may display reduced oxygen tension thereby forcing tumor cells to infiltrate the surrounding brain parenchyma. This is also supported by recent data from our laboratory showing a significant increase in lactate levels in the infiltrative tumor by NMR spectroscopy (24). The cell-to-cell signaling and interaction network extracted from the angiogenic tumor suggests an increased cross-talk between tumor cells and/or between tumor and host cells. This may reflect a better adaptation of the cancer cells to their microenvironment in the angiogenic phenotype, thereby favoring the induction of new blood vessels and improved tumor growth. Based on the protein IDs of this network (AnxA3, Calnexin, interferon α, MHC class I, and NFκB), an interaction between tumor cells and the host immune system is also conceivable. Thus our data suggest that enhanced tumor host interaction may lead to a better adaptation of the tumor to its microenvironment, which may form the basis for the angiogenic switch in solid tumors. The precise analysis of the candidate proteins in this cross-talk will provide clues on the role of the environment on tumor progression.

In conclusion, based on a novel clinically highly relevant xenograft brain tumor model, we have generated an extensive and unique data set of protein expression profiles that recapitulates the change from invasive to angiogenic tumor growth. Based on glioma TMA expression analysis, we propose Calnexin, AnxA2, and AnxA5 as novel biomarkers for high grade gliomas. Pathway analysis suggests the importance of increased metabolic activity and tumor host interactions to drive tumor growth in the angiogenic phenotype. The evaluation phase of the candidate proteins should reveal novel biomarkers that can be further exploited as therapeutic targets for malignant gliomas.

REFERENCES

1. Louis, D. N., Ohgaki, H., Wiestler, O. D., Cavenee, W. K., Burger, P. C., Jouvet, A., Scheithauer, B. W., and Kleihues, P. (2007) The 2007 WHO classification of tumours of the central nervous system. *Acta Neuropathol.* **114,** 97–109
2. Hoelzinger, D. B., Demuth, T., and Berens, M. E. (2007) Autocrine factors that sustain glioma invasion and paracrine biology in the brain microenvironment. *J. Natl. Cancer Inst.* **99,** 1583–1593

3. Carmeliet, P., and Jain, R. K. (2000) Angiogenesis in cancer and other diseases. *Nature* **407,** 249–257

4. Jain, R. K., di Tomaso, E., Duda, D. G., Loeffler, J. S., Sorensen, A. G., and Batchelor, T. T. (2007) Angiogenesis in brain tumours. *Nat. Rev. Neurosci.* **8,** 610–622

5. Reiss, Y., Machein, M. R., and Plate, K. H. (2005) The role of angiopoietins during angiogenesis in gliomas. *Brain Pathol.* **15,** 311–317

6. Reardon, D. A., Wen, P. Y., Desjardins, A., Batchelor, T. T., and Vredenburgh, J. J. (2008) Glioblastoma multiforme: an emerging paradigm of anti-VEGF therapy. *Expert Opin. Biol. Ther.* **8,** 541–553

7. Hanahan, D., and Folkman, J. (1996) Patterns and emerging mechanisms of the angiogenic switch during tumorigenesis. *Cell* **86,** 353–364

8. Sakariassen, P. Ø., Prestegarden, L., Wang, J., Skaftnesmo, K. O., Mahesparan, R., Molthoff, C., Sminia, P., Sundlisaeter, E., Misra, A., Tysnes, B. B., Chekenya, M., Peters, H., Lende, G., Kalland, K. H., Øyan, A. M., Petersen, K., Jonassen, I., van der Kogel, A., Feuerstein, B. G., Terzis, A. J., Bjerkvig, R., and Enger, P. Ø. (2006) Angiogenesis-independent tumor growth mediated by stem-like cancer cells. *Proc. Natl. Acad. Sci. U.S.A.* **103,** 16466–16471

9. Rajcevic, U., Niclou, S. P., and Jimenez, C. R. (2009) Proteomics strategies for target identification and biomarker discovery in cancer. *Front. Biosci.* **14,** 3292–3303

10. Li, K. W., Miller, S., Klychnikov, O., Loos, M., Stahl-Zeng, J., Spijker, S., Mayford, M., and Smit, A. B. (2007) Quantitative proteomics and protein network analysis of hippocampal synapses of CaMKIIalpha mutant mice. *J. Proteome Res.* **6,** 3127–3133

11. Hopkins, A. L., and Groom, C. R. (2003) Target analysis: a priori assessment of druggability. *Ernst Schering Res. Found. Workshop* **42,** 11–17

12. Josic, D., and Clifton, J. G. (2007) Mammalian plasma membrane proteomics. *Proteomics* **7,** 3010–3029

13. Josic, D., Clifton, J. G., Kovac, S., and Hixson, D. C. (2008) Membrane proteins as diagnostic biomarkers and targets for new therapies. *Curr. Opin. Mol. Ther.* **10,** 116–123

14. Rabilloud, T. (2003) Membrane proteins ride shotgun. *Nat. Biotechnol.* **21,** 508–510

15. Mahesparan, R., Read, T. A., Lund-Johansen, M., Skaftnesmo, K. O., Bjerkvig, R., and Engebraaten, O. (2003) Expression of extracellular matrix components in a highly infiltrative in vivo glioma model. *Acta Neuropathol.* **105,** 49–57

16. Bjerkvig, R., Tønnesen, A., Laerum, O. D., and Backlund, E. O. (1990) Multicellular tumor spheroids from human gliomas maintained in organ culture. *J. Neurosurg.* **72,** 463–475

17. Li, K., Hornshaw, M. P., van Minnen, J., Smalla, K. H., Gundelfinger, E. D., and Smit, A. B. (2005) Organelle proteomics of rat synaptic proteins: correlation-profiling by isotope-coded affinity tagging in conjunction with liquid chromatography-tandem mass spectrometry to reveal post-synaptic density specific proteins. *J. Proteome Res.* **4,** 725–733

18. Dysvik, B., and Jonassen, I. (2001) J-Express: exploring gene expression data using Java. *Bioinformatics* **17,** 369–370

19. Stavrum, A. K., Petersen, K., Jonassen, I., and Dysvik, B. (2008) Analysis of gene-expression data using J-Express. *Curr. Protoc. Bioinformatics* Chapter 7, Unit 7.3

20. Breitling, R., Armengaud, P., Amtmann, A., and Herzyk, P. (2004) Rank products: a simple, yet powerful, new method to detect differentially regulated genes in replicated microarray experiments. *FEBS Lett.* **573,** 83–92

21. Fellenberg, K., Hauser, N. C., Brors, B., Neutzner, A., Hoheisel, J. D., and Vingron, M. (2001) Correspondence analysis applied to microarray data. *Proc. Natl. Acad. Sci. U.S.A.* **98,** 10781–10786

22. Tamayo, P., Slonim, D., Mesirov, J., Zhu, Q., Kitareewan, S., Dmitrovsky, E., Lander, E. S., and Golub, T. R. (1999) Interpreting patterns of gene expression with self-organizing maps: methods and application to hematopoietic differentiation. *Proc. Natl. Acad. Sci. U.S.A.* **96,** 2907–2912

23. Goplen, D., Wang, J., Enger, P. Ø., Tysnes, B. B., Terzis, A. J., Laerum, O. D., and Bjerkvig, R. (2006) Protein disulfide isomerase expression is related to the invasive properties of malignant glioma. *Cancer Res.* **66,** 9895–9902

24. Thorsen, F., Jirak, D., Wang, J., Sykova, E., Bjerkvig, R., Enger, P. Ø., van der Kogel, A., and Hajek, M. (2008) Two distinct tumor phenotypes isolated from glioblastomas show different MRS characteristics. *NMR Biomed.* **21,** 830–838

25. Bedard, K., Szabo, E., Michalak, M., and Opas, M. (2005) Cellular functions of endoplasmic reticulum chaperones calreticulin, calnexin, and ERp57. *Int. Rev. Cytol.* **245,** 91–121

26. Zhang, Y., and Williams, D. B. (2006) Assembly of MHC class I molecules within the endoplasmic reticulum. *Immunol. Res.* **35,** 151–162

27. Park, J. E., Lee, D. H., Lee, J. A., Park, S. G., Kim, N. S., Park, B. C., and Cho, S. (2005) Annexin A3 is a potential angiogenic mediator. *Biochem. Biophys. Res. Commun.* **337,** 1283–1287

28. Junker, H., Suofu, Y., Venz, S., Sascau, M., Herndon, J. G., Kessler, C., Walther, R., and Popa-Wagner, A. (2007) Proteomic identification of an upregulated isoform of annexin A3 in the rat brain following reversible cerebral ischemia. *Glia* **55,** 1630–1637

29. Konishi, H., Namikawa, K., and Kiyama, H. (2006) Annexin III implicated in the microglial response to motor nerve injury. *Glia* **53,** 723–732

30. Roseman, B. J., Bollen, A., Hsu, J., Lamborn, K., and Israel, M. A. (1994) Annexin II marks astrocytic brain tumors of high histologic grade. *Oncol. Res.* **6,** 561–567

31. Ling, Q., Jacovina, A. T., Deora, A., Febbraio, M., Simantov, R., Silverstein, R. L., Hempstead, B., Mark, W. H., and Hajjar, K. A. (2004) Annexin II regulates fibrin homeostasis and neoangiogenesis in vivo. *J. Clin. Investig.* **113,** 38–48

32. Sharma, M. C., and Sharma, M. (2007) The role of annexin II in angiogenesis and tumor progression: a potential therapeutic target. *Curr. Pharm. Des.* **13,** 3568–3575

33. Yan, L., Zucker, S., and Toole, B. P. (2005) Roles of the multifunctional glycoprotein, emmprin (basigin; CD147), in tumour progression. *Thromb. Haemost.* **93,** 199–204

34. Ohgaki, H., and Kleihues, P. (2007) Genetic pathways to primary and secondary glioblastoma. *Am. J. Pathol.* **170,** 1445–1453

35. Shinojima, N., Tada, K., Shiraishi, S., Kamiryo, T., Kochi, M., Nakamura, H., Makino, K., Saya, H., Hirano, H., Kuratsu, J., Oka, K., Ishimaru, Y., and Ushio, Y. (2003) Prognostic value of epidermal growth factor receptor in patients with glioblastoma multiforme. *Cancer Res.* **63,** 6962–6970

36. Lund-Johansen, M., Bjerkvig, R., Humphrey, P. A., Bigner, S. H., Bigner, D. D., and Laerum, O. D. (1990) Effect of epidermal growth factor on glioma cell growth, migration, and invasion in vitro. *Cancer Res.* **50,** 6039–6044